

Research Article

Xu-Hao Huang, Jian Yang*, Iftikhar Azim, Xin Ren, and Xing-er Wang

Static and dynamic analyses of auxetic hybrid FRC/CNTRC laminated plates

<https://doi.org/10.1515/ntrev-2020-0106>

received November 26, 2020; accepted December 9, 2020

Abstract: In this work, a hybrid laminated plate is developed by changing ply orientations and stacking sequences. The hybrid laminated plate is composed of carbon nanotube reinforced composite and fiber reinforced composite layers. Negative Poisson's ratio (NPR) is obtained for the case of $[22^F/(22^C/-22^C)_{3T}/-22^F]$ laminate. A theoretical laminated model considering geometric nonlinearity and shear deformation is presented. Based on a two-step perturbation method, the solutions of the motion equations are obtained to capture the nonlinear frequencies and load–deflection curves. On this basis, the fourth-order Runge–Kutta method is used to obtain the dynamic response of hybrid laminated plates. The presented model is verified by comparing the results obtained analytically and numerically. Several factors such as loading and distribution of carbon nanotubes (CNTs), and foundation type are considered in parametric study. Numerical results indicate that the thermal-mechanical behavior of hybrid laminated plates significantly improved by properly adjusting the CNT distribution. In addition, the results reveal that changes in temperature and foundation stiffness have pronounced influence on the nonlinear vibration characteristics of

hybrid laminate plates with NPR as compared to those with positive Poisson's ratio.

Keywords: auxetic, hybrid laminated plate, nonlinear dynamics, nonlinear bending, CNT reinforced composite, temperature-dependent properties

1 Introduction

Structures made from auxetic materials are becoming important in many industries because of the inherent excellent properties of these materials. Because of developments in the manufacturing technology, various auxetic materials and structures are developed and fabricated nowadays [1–3]. Ren *et al.* [4] performed a systematic review of these structures. Recently, the studies on the design and mechanical analyses have propelled to achieve improvements in the mechanical properties of the auxetic structures such as impact resistance [5–7] and energy absorption [8,9]. Furthermore, these structural elements require high reliability in their service life as the plates easily damage under different loading scenarios. For a safe design, the necessity of accurate evaluation of the mechanical behaviors of such plates is becoming inevitable. The characterization of the static and dynamic response is also required to estimate the frequencies and deflections of auxetic plates under different environmental scenarios. A number of studies have been dedicated to these structures. Particularly, investigations were made to study the bending [10,11], dynamic [12,13], and buckling behavior [13–15] of these structures. However, in these researches [10–15], the value of the negative Poisson's ratios (NPRs) for estimating the effect of auxetic feature on the mechanical behavior of a plate is based on an assumption.

In the design of auxetic laminates, the concept of engineering constants is usually introduced to characterize the effective performance of these laminates. Evans *et al.* [16] found that effective NPR can be obtained by adjusting layup sequences in the laminates. Zhang *et al.* [17] also found that both the layup sequence and

* **Corresponding author: Jian Yang**, State Key Laboratory of Ocean Engineering, Shanghai Jiao Tong University, Shanghai 200240, China; Shanghai Key Laboratory for Digital Maintenance of Buildings and Infrastructure, School of Naval Architecture, Ocean and Civil Engineering, Shanghai Jiao Tong University, Shanghai 200240, China; School of Civil Engineering, University of Birmingham, Birmingham B15 2TT, United Kingdom, e-mail: j.yang.3@bham.ac.uk

Xu-Hao Huang, Iftikhar Azim, Xing-er Wang: State Key Laboratory of Ocean Engineering, Shanghai Jiao Tong University, Shanghai 200240, China; Shanghai Key Laboratory for Digital Maintenance of Buildings and Infrastructure, School of Naval Architecture, Ocean and Civil Engineering, Shanghai Jiao Tong University, Shanghai 200240, China

Xin Ren: College of Civil Engineering, Nanjing Tech University (Nanjing Tech), Nanjing 211816, China

anisotropic material are necessary for structures to exhibit an NPR. In addition, many investigations are conducted regarding fiber reinforced composite (FRC) laminates with NPR. Herakovich [18] studied the auxetic behavior of $(\pm\theta)_s$ laminates and found that the NPR of $(\pm 25)_s$ laminate is -0.21 . Hine *et al.* [19] observed that composites made with a high modulus carbon fiber are obtained to exhibit NPR value of ν_{23} of 0.5 . Matsuda *et al.* [20] reported that the maximum amplitude of NPR in FRC laminates was close to -0.7 when the laying angle is 25° . Harkati *et al.* [21,22] investigated the effect of material properties on ν_{13}^e of a symmetric $(\theta/-\theta)_{2s}$ plate. It was shown that the NPR of Kevlar and carbon reinforced composite plate was -0.746 at $\theta = 20^\circ$. Most of the above studies reveal that the magnitude of NPR of the laminated structures greatly depends on their laying angle and stacking sequences [23].

FRCs are applied in the design of laminates with NPR. Compared with FRCs, carbon nanotube reinforced composite (CNTRC) has the advantages of high strength and strong anisotropy. In addition, functionally graded (FG) materials are frequently used in many fields. Combining the concept of FG with carbon nanotubes (CNTs) can be used to improve the performance of CNTRC [24]. Based on the design of auxetic FRC laminates, this concept is applied to the design of FRC/CNTRC hybrid laminate with NPR. This hybrid laminate is made of FG-CNTRC core and FRC face sheets. Shen [24] proposed the concept of FG-CNTRC structures and studied the mechanical behavior of these structures at different scales. Thereafter, researches on the static and vibration response of FG-CNTRC structures were carried out [25–29]. Fan and Wang [27] used a theoretical model together with a finite element approach to analyze low-velocity impact response of the FG-CNTRC beams. Chen *et al.* [29] used the third-order piston theory to study the thermal buckling behavior of multi-scale hybrid laminated nanocomposite disk exposed to hygro-mechanical loading. Fu *et al.* [30,31] examined the dynamic instability of FG-CNTRC and FGM conical shells in the framework of first-order shear deformation theory. Yang and his coauthors studied the effects of out-of-plane NPR on the nonlinear flexural and dynamic behavior of FG-CNTRC structures [32,33]. Yu and Shen [34] investigated the nonlinear mechanical behavior of hybrid metal/CNTRC plate resting on elastic foundations. By considering the matrix cracks, Fan *et al.* [35,36] studied the static and dynamic characteristics of hybrid laminated structures made from either FRC or CNTRC. Lei *et al.* [37,38] investigated the influence of matrix cracks on the bending and vibration behavior of FRC/CNTRC plates using the element-free Galerkin

method and self-consistent model. Further, the buckling behavior of these structures was examined by Lei and Yang [39]. Kamarian *et al.* [40] used the firefly algorithm for the optimization of fiber/CNT/polymer plates to maximize the natural frequency. Furthermore, the adoption of FRC/CNTRC hybrid concept was later extended to the design of composite blades by Zhang *et al.* [41,42]. They are concerned with the nonlinear vibration responses of hybrid composite blades. In addition, the studies of the hybrid laminated structures made with multi-materials can be found in ref. [43–51]. However, there are no studies available in literature that report the vibration and dynamic characteristics of auxetic FRC/CNTRC hybrid laminated plate.

In the present study, both FRC/CNTRC hybrid configurations and NPR are considered. The authors used Reddy Shear Deformation Theory with von Kármán nonlinear theory for bending, vibration, and forced vibration analyses of these structures. The motion equations are derived by considering temperature field and subgrade reaction of foundation. The effects of the CNT configuration, environmental conditions, and foundation type on the mechanical behavior of hybrid laminated plate with NPR or positive Poisson's ratio (PPR) are assessed.

2 Theoretical modeling of hybrid laminates with NPR or PPR

2.1 Effective Poisson's ratio for laminates

The global stiffness and strength of laminates depend on the ply orientation and stacking sequence. The effect of CNTs' orientation angle on the instability characteristic of laminated plate is studied by Liew *et al.* [52] and Jam and Maghamikia [53]. It was assumed in these studies that reinforcing fibers are of sufficient length to be laid in at different angles. The same assumption is also considered in the current work.

Sun and Li [23] presented a model for effective Poisson's ratio (EPR) of symmetric laminates. This model cannot be applied for an arbitrary layup laminates. Unlike the Sun *et al.*'s model [23], the model proposed in this study considers the effect of bending and bending-extension coupling, and provide more accurate prediction of EPR of an arbitrary angle-ply laminates. Based on the classical laminate theory, the formulae for the EPR are obtained as follows:

$$v_{13}^e = - \left| \begin{array}{cc} \mathbf{A}_{1,2} & \mathbf{B}_{2,3}^T \\ \mathbf{B}_{1,2} & \mathbf{D} \end{array} \right| \left/ \left| \begin{array}{cc} \mathbf{A}_{2,3} & \mathbf{B}_{2,3}^T \\ \mathbf{B}_{2,3} & \mathbf{D} \end{array} \right| \right|, \quad (1)$$

$$\mathbf{A}_{m,n} = \begin{bmatrix} A_{2n} & A_{2m} & 0 & 0 & A_{26} \\ A_{3n} & A_{3m} & 0 & 0 & A_{36} \\ 0 & 0 & A_{44} & A_{45} & 0 \\ 0 & 0 & A_{45} & A_{55} & 0 \\ A_{6n} & A_{6m} & 0 & 0 & A_{66} \end{bmatrix},$$

$$\mathbf{B}_{m,n} = \begin{bmatrix} B_{1n} & B_{1m} & 0 & 0 & B_{16} \\ B_{2n} & B_{2m} & 0 & 0 & B_{26} \\ B_{3n} & B_{3m} & 0 & 0 & B_{36} \\ 0 & 0 & B_{44} & B_{45} & 0 \\ 0 & 0 & B_{45} & B_{55} & 0 \\ B_{6n} & B_{6m} & 0 & 0 & B_{66} \end{bmatrix}, \quad (2)$$

$$(m, n) = (1, 2; 2, 3)$$

$$\mathbf{D} = \begin{bmatrix} D_{11} & D_{12} & D_{13} & 0 & 0 & D_{16} \\ D_{21} & D_{22} & D_{23} & 0 & 0 & D_{26} \\ D_{31} & D_{32} & D_{33} & 0 & 0 & D_{36} \\ 0 & 0 & 0 & D_{44} & D_{45} & 0 \\ 0 & 0 & 0 & D_{45} & D_{55} & 0 \\ D_{61} & D_{62} & D_{63} & 0 & 0 & D_{66} \end{bmatrix},$$

where $\mathbf{B}_{2,3}^T$ is the transposed matrix of $\mathbf{B}_{2,3}$, and A_{ij} , B_{ij} , D_{ij} , ($i, j = 1-6$) are the stiffnesses of laminates, given in ref. [54]. When considering an antisymmetric angle-ply laminated plate with UD or FG-O and FG-X configurations, a simplified form of equation (1) can be found in previous work [55]. Details about the derivation process of EPRs are found in ref. [27] and [56].

Furthermore, the presented model has high generalization capacity because it can be used to design symmetric laminates as well as laminates with asymmetric materials properties. In the current work, FRC/CNTRC hybrid laminate with NRP is developed. The hybrid laminated plates are modeled in the hinged condition with the following ply orientation and stacking sequence: $[\theta^F/(\theta^C/-\theta^C)_{3T}/-\theta^F]$. To facilitate the identification, the superscript F and C represent the layer of FRC and CNTRC,

respectively. To predict the EPR of hybrid laminate, the material parameters of each layer are determined. Based on ref. [24] and [57], the general form for calculating these properties are given by Fan and Wang [36], which can be expressed as:

$$E_{11} = \eta_1 V_r E_{11}^r + V_m E^m,$$

$$E_{22} = \eta_2 \left/ \left(\frac{V_r}{E_{22}^r} + \frac{V_m}{E^m} \right) - \eta_4 V_r V_m \frac{V_r^2 E^m / E_{22}^r + V_m^2 E_{22}^r / E^m - 2v_r v_m}{V_r E_{22}^r + V_m E^m} \right|, \quad (3a)$$

$$G_{12} = \eta_3 \left/ \left(\frac{V_r}{G_{12}^r} + \frac{V_m}{G^m} \right) \right|,$$

$$\alpha_{11} = \frac{V_r E_{11}^r \alpha_{11}^r + V_m E^m \alpha^m}{V_r E_{11}^r + E^m \alpha^m}, \quad (3b)$$

$$\alpha_{22} = (1 - v_{12}^r) V_r \alpha_{22}^r + (1 - v^m) V_m \alpha^m - v_{12} \alpha_{11}. \quad (3c)$$

η_i ($i = 1, 2, 3, 4$) are the efficiency coefficients, and ρ and α_{ii} ($i = 1, 2$) are the density and thermal expansion coefficients of composite material, respectively. The Poisson's ratio (v_{12}) is obtained as:

$$\rho = V_r \rho^r + V_m \rho^m, \quad (4a)$$

$$v_{12} = V_r v_{12}^r + V_m v^m = V_r v_{12}^r + (1 - V_r) v^m, \quad (4b)$$

where the superscript r ($r = \text{CNT}, \text{F}$) means reinforcement and subscript m means matrix; E_{11}^r and E_{22}^r are the longitudinal and transverse moduli of elasticity; G_{12}^r is the shear moduli in the X - Y planes; and V_r denotes the volume of the constituent. E^m is the elastic modulus of isotropic matrix. The material properties of the fiber are: $E_{11}^F = 233.05 \text{ GPa}$, $\alpha_{11}^F = -5.4 \times 10^{-7} \text{ K}^{-1}$, $v_{12}^F = 0.2$, $E_{22}^F = 23.1 \text{ GPa}$, $\alpha_{22}^F = 10.08 \times 10^{-6} \text{ K}^{-1}$, $G_{12}^F = 8.96 \text{ GPa}$, $\rho^F = 1,750 \text{ kg/m}^3$. The properties that relate CNT/PmPV are reported in ref. [24,25] and are summarized in Tables 1 and 2.

The analytical solution mentioned above is capable of calculating the EPR of an arbitrary angle-ply laminate. A systematic investigation of the antisymmetric hybrid laminates is also carried out. Five configurations of laminated plates are considered as described in Table 3, and the uniform distribution (UD) is used as a reference. These configurations are for an identical material and

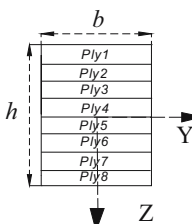
Table 1: Temperature-dependent properties of CNT/PmPV ($v_{12}^{\text{CNT}} = 0.175$, $v^m = 0.34$) [24,25]

T (K)	E_{11}^{CNT} (TPa)	E_{22}^{CNT} (TPa)	G_{12}^{CNT} (TPa)	E^m (TPa)	α_{11}^{CNT} ($10^{-6}/\text{K}$)	α_{22}^{CNT} ($10^{-6}/\text{K}$)	α^m ($10^{-5}/\text{K}$)
300	5.6466	7.0800	1.9445	2.1000	3.4584	5.1682	4.500
400	5.5679	6.9814	1.9703	1.6300	4.1496	5.0905	4.725
500	5.5308	6.9348	1.9643	1.1600	4.5361	5.0189	4.950

Table 2: Values of the efficiency parameters η_j ($j = 1, 2, 3, 4$) [24,45]

Volume fraction (V_f)	$V_{CNT} = 0.11$	$V_{CNT} = 0.14$	$V_{CNT} = 0.17$	$V_F = 0.6$
η_1	0.149	0.15	0.15	1
η_2	0.934	0.941	0.941	1
η_3	0.934	0.941	0.941	1
η_4	0	0	0	1

Table 3: Configuration of CNT for FRC/CNTRC laminate plate

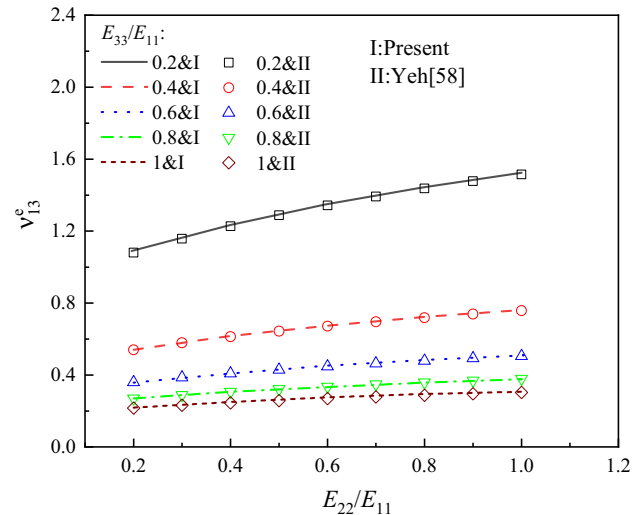
Types of ply	UD	FG-X	FG-O	FG-Λ	FG-V	Geometry of laminated plate
Ply1	0.6	0.6	0.6	0.6	0.6	
Ply2	0.14	0.17	0.11	0.11	0.17	
Ply3	0.14	0.14	0.14	0.11	0.17	
Ply4	0.14	0.11	0.17	0.14	0.14	
Ply5	0.14	0.11	0.17	0.14	0.14	
Ply6	0.14	0.14	0.14	0.17	0.11	
Ply7	0.14	0.17	0.11	0.17	0.11	
Ply8	0.6	0.6	0.6	0.6	0.6	

have a constant thickness of 0.125 and 0.25 mm for FRC and CNT layers, respectively. Several types of CNT distributions are taken into consideration, which include the type of CNT volume fraction (V_{CNT}) and the volume fraction of the fibers to be fixed as $V_F = 0.6$ (see Figure 3(b)).

2.2 Design of auxetic hybrid laminate

An analytical example is given to show the correctness of the solutions mentioned above. Figure 1 shows the comparison of the solutions of the EPR (v_{13}^e) and the solution derived by Yeh *et al.* [58] for a symmetric laminate. The material parameters of the laminates are $E_{11} = 200$ GPa, $\nu_{12} = 0.2$, $\nu_{31} = 0.4$, $\nu_{32} = 0.6$, and $G_{12}/E_{11} = 0.2$. EPRs (v_{13}^e) have been predicted for a wide range of elastic modulus ratio E_{33}/E_{11} . In Figure 1, the values of v_{13}^e for symmetric laminates are plotted with varying relative elastic modulus E_{22}/E_{11} . It can be noted that the EPRs (v_{13}^e) calculated by the proposed method agrees well with those obtained by Yeh *et al.* [58].

Here, equation (1) is adopted to assess the effect of the ply orientations and FG configuration on the EPR (v_{13}^e). Figure 2 shows the effect of the CNT and fiber orientation θ on the EPR of the $[\theta^F/(\theta^C/(-\theta^C)_{3T}/-\theta^F)]$ laminated plates. It is observed that v_{13}^e decreases with increasing θ . v_{13}^e attains its minimum and maximum negative values at θ equal to 22° and 90° , respectively, whereas the value of v_{13}^e is positive at $\theta = 45^\circ$. As expected, the ply orientation significantly affects the EPR of hybrid laminated plates. In this regard, $[22^F/(22^C/-22^C)_{3T}/-22^F]$ and $[45^F/(45^C/-45^C)_{3T}/-45^F]$ are taken as example.

**Figure 1:** Effect of E_{22}/E_{11} on the EPR (v_{13}^e) of laminates $(45^F/-45^F)_{4S}$.

$[22^F/(22^C/-22^C)_{3T}/-22^F]$ laminate is negative, whereas $[45^F/(45^C/-45^C)_{3T}/-45^F]$ plate has PPR. The results in terms of EPR of these hybrid laminates and the corresponding FG configurations are presented in Table 4.

3 Theoretical modeling of nonlinear behavior

3.1 Motion equations

Laminates consist of layers of composites reinforced with CNTRC and FRC. Consider a hybrid laminated plate composed of eight layers with lamination scheme $[\theta^F/(\theta^C/$

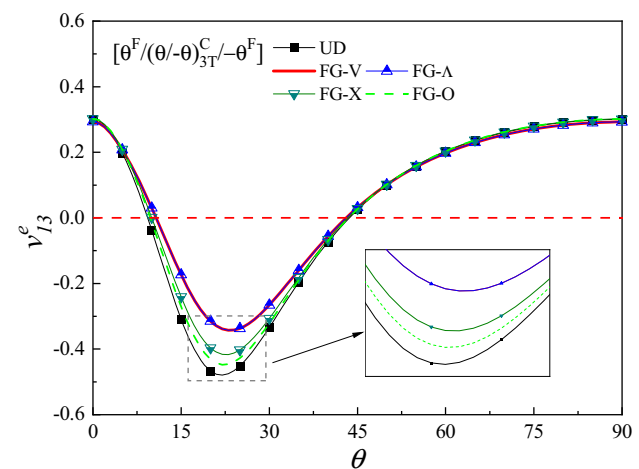
**Figure 2:** EPR (v_{13}^e)-laying angle for $[\theta^F/(\theta^C/(-\theta^C)_{3T}/-\theta^F]$ laminated plates.

Table 4: EPR (v_{13}^e) of hybrid laminates for various temperature conditions

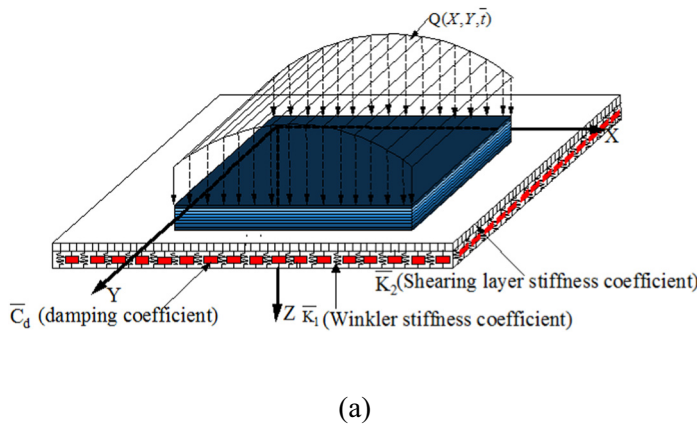
FG-	$[22^F/(22^C/-22^C)_{3T}/-22^F]$			$[45^F/(45^C/-45^C)_{3T}/-45^F]$		
	300 K	400 K	500 K	300 K	400 K	500 K
UD	-0.479	-0.580	-0.723	0.025	0.020	0.015
FG-V	-0.338	-0.427	-0.559	0.031	0.026	0.019
FG-Λ	-0.338	-0.427	-0.559	0.031	0.026	0.019
FG-X	-0.416	-0.515	-0.658	0.028	0.023	0.017
FG-O	-0.447	-0.548	-0.693	0.027	0.022	0.016

$-\theta^C)_{3T}/\theta^F]$ and resting on a continuous elastic and visco-elastic foundation as shown in Figure 3. Figure 3(a) defines the coordinate system used in the analysis of hybrid laminated plate analysis. The XYZ coordinate system is assumed to have its origin on the middle face of the plate, so that the middle surface lies in the XY-plane. The displacements at a point in the X, Y, and Z directions are \bar{U} , \bar{V} , and \bar{W} , respectively.

The simply supported plate is surrounded by a visco-Pasternak foundation that consists of the Winkler foundation (\bar{K}_1), shearing layer stiffness (\bar{K}_2), and visco-elastic foundation (\bar{C}_d). The distributed reaction between this foundation and the bottom layer of the hybrid plate can be expressed as:

$$p_0(X, Y, t) = \bar{K}_1 \bar{W} - \bar{K}_2 (\partial^2 \bar{W} / \partial X^2 + \partial^2 \bar{W} / \partial Y^2) + \bar{C}_d \partial \bar{W} / \partial t. \quad (5)$$

The method of analysis is based on the third-order shear deformation theory [59] for the laminated plate undergoing large deflection. The effect of the elevated temperature is considered by introducing thermal forces \bar{N}^T , moments \bar{M}^T , and higher order moments \bar{P}^T , as defined in Appendix A. For the forced vibration problem, the applied load Q is considered. The motion equations are written as follows:



$$\begin{aligned} & \tilde{L}_{11}(\bar{W}) - \tilde{L}_{12}(\bar{\Psi}_x) - \tilde{L}_{13}(\bar{\Psi}_y) + \tilde{L}_{14}(\bar{F}) - \tilde{L}_{15}(\bar{N}^T) - \tilde{L}_{16}(\bar{M}^T) + p_0 \\ & = \tilde{L}_{17}(\ddot{\bar{W}}) + \tilde{L}(\bar{W}, \bar{F}) + I_8 \left(\frac{\partial \ddot{\bar{\Psi}}_x}{\partial X} + \frac{\partial \ddot{\bar{\Psi}}_y}{\partial Y} \right) + Q, \end{aligned} \quad (6)$$

$$\tilde{L}_{21}(\bar{F}) + \tilde{L}_{22}(\bar{\Psi}_x) + \tilde{L}_{23}(\bar{\Psi}_y) - \tilde{L}_{24}(\bar{W}) - \tilde{L}_{25}(\bar{N}^T) = -\frac{1}{2} \tilde{L}(\bar{W}, \bar{W}), \quad (7)$$

$$\begin{aligned} & \tilde{L}_{31}(\bar{W}) + \tilde{L}_{32}(\bar{\Psi}_x) - \tilde{L}_{33}(\bar{\Psi}_y) + \tilde{L}_{34}(\bar{F}) - \tilde{L}_{35}(\bar{N}^T) \\ & - \tilde{L}_{36}(\bar{S}^T) = I_9 \frac{\partial \ddot{\bar{W}}}{\partial X} + I_{10} \ddot{\bar{\Psi}}_x, \end{aligned} \quad (8)$$

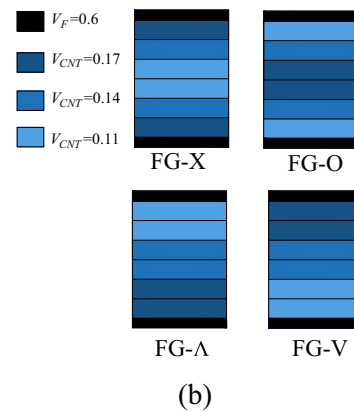
$$\begin{aligned} & \tilde{L}_{41}(\bar{W}) - \tilde{L}_{42}(\bar{\Psi}_x) + \tilde{L}_{43}(\bar{\Psi}_y) + \tilde{L}_{44}(\bar{F}) - \tilde{L}_{45}(\bar{N}^T) \\ & - \tilde{L}_{46}(\bar{S}^T) = I_9 \frac{\partial \ddot{\bar{W}}}{\partial Y} + I_{10} \ddot{\bar{\Psi}}_y, \end{aligned} \quad (9)$$

where the nonlinear operator ($\tilde{L}()$) and the stress function (\bar{F}) can be expressed as follows:

$$\tilde{L}() = \frac{\partial^2}{\partial X^2} \frac{\partial^2}{\partial Y^2} + \frac{\partial^2}{\partial Y^2} \frac{\partial^2}{\partial X^2} - 2 \frac{\partial^2}{\partial X \partial Y} \frac{\partial^2}{\partial X \partial Y}, \quad (10)$$

$$\bar{N}_x = \frac{\partial^2 \bar{F}}{\partial Y^2}, \quad \bar{N}_{xy} = \frac{\partial^2 \bar{F}}{\partial X \partial Y}, \quad \bar{N}_y = \frac{\partial^2 \bar{F}}{\partial X^2}, \quad (11)$$

where $\bar{\psi}_x$ and $\bar{\psi}_y$ denote the rotation about the Y- and X-axes. The coefficients S_{ij} and inertias I_i are shown in Appendix A. The operators ($\tilde{L}_{ij}()$) introduced in the above motion equations are defined from ref. [60].

**Figure 3:** Coordinate system and various configurations of hybrid laminated plates.

In the current work, simply supported boundary conditions (BCs) are used.

At $X = 0, a$:

$$\bar{W} = \bar{\Psi}_y = \bar{M}_x = \bar{P}_x = 0, \quad (12a)$$

$$\bar{U} = 0, \quad (12b)$$

At $Y = 0, b$:

$$\bar{W} = \bar{\Psi}_x = \bar{M}_y = \bar{P}_y = 0, \quad (12c)$$

$$\bar{V} = 0, \quad (12d)$$

where \bar{M}_x, \bar{P}_x ($i = x, y$) are the bending and higher order moments, respectively, shown in ref. [60]. \bar{U} and \bar{V} are the plate displacements in X and Y directions.

The immovable in-plane BCs (12b) and (12d) are converted to integral form as given below:

$$\int_0^b \int_0^a \partial \bar{U} / \partial X \, dX dY = 0, \quad (13a)$$

$$\int_0^a \int_0^b \partial \bar{V} / \partial Y \, dY dX = 0, \quad (13b)$$

where,

$$\begin{aligned} \frac{\partial \bar{U}}{\partial X} = & A_{11}^* \left(\frac{\partial^2 \bar{F}}{\partial Y^2} - \bar{N}_x^T \right) + \left(B_{12}^* - \frac{4E_{12}^*}{3h^2} \right) \frac{\partial \bar{\Psi}_y}{\partial Y} + A_{12}^* \left(\frac{\partial^2 \bar{F}}{\partial X^2} - \bar{N}_y^T \right) \\ & + \left(B_{11}^* - \frac{4E_{11}^*}{3h^2} \right) \frac{\partial \bar{\Psi}_x}{\partial X} - \frac{4}{3h^2} \left(E_{21}^* \frac{\partial^2 \bar{W}}{\partial X^2} + E_{22}^* \frac{\partial^2 \bar{W}}{\partial Y^2} \right) - \frac{1}{2} \left(\frac{\partial \bar{W}}{\partial X} \right)^2, \end{aligned} \quad (14a)$$

$$\begin{aligned} \frac{\partial \bar{V}}{\partial Y} = & A_{22}^* \left(\frac{\partial^2 \bar{F}}{\partial X^2} - \bar{N}_y^T \right) + A_{12}^* \left(\frac{\partial^2 \bar{F}}{\partial Y^2} - \bar{N}_x^T \right) + \left(B_{21}^* - \frac{4E_{21}^*}{3h^2} \right) \frac{\partial \bar{\Psi}_x}{\partial X} \\ & + \left(B_{22}^* - \frac{4E_{22}^*}{3h^2} \right) \frac{\partial \bar{\Psi}_y}{\partial Y} - \frac{4}{3h^2} \left(E_{21}^* \frac{\partial^2 \bar{W}}{\partial X^2} + E_{22}^* \frac{\partial^2 \bar{W}}{\partial Y^2} \right) - \frac{1}{2} \left(\frac{\partial \bar{W}}{\partial X} \right)^2, \end{aligned} \quad (14b)$$

in which the reduced stiffnesses of plate ($A_{ij}^*, B_{ij}^*, D_{ij}^*, E_{ij}^*, F_{ij}^*, H_{ij}^*$) are the functions of the geometry, materials properties, and stacking sequence of the laminated plate as given in Appendix A.

The nonlinear motion equations for the forced vibration can be solved by a two-step perturbation approach proposed by Shen [60]. Equations (6)–(9) can be converted to dimensionless forms by the definition of the following dimensionless parameters as:

$$\begin{aligned} L_{11}(W) - L_{12}(\Psi_x) - L_{13}(\Psi_y) + \gamma_{14} L_{14}(F) - L_{16}(M^T) \\ = L_{17}(\ddot{W}) + \lambda_q - K_1 W + K_2 \nabla^2 W - C_d \frac{\partial W}{\partial t} \\ + \gamma_{14} \beta^2 L(W, F) + \gamma_{80} \left(\frac{\partial \ddot{\Psi}_x}{\partial x} + \beta \frac{\partial \ddot{\Psi}_y}{\partial y} \right), \end{aligned} \quad (15)$$

$$\begin{aligned} L_{21}(F) + \gamma_{24} [L_{22}(\Psi_x) + L_{23}(\Psi_y) - L_{24}(W)] \\ = -\frac{1}{2} \gamma_{24} \beta^2 L(W, W), \end{aligned} \quad (16)$$

$$\begin{aligned} L_{31}(W) + L_{32}(\Psi_x) - L_{33}(\Psi_y) + \gamma_{14} L_{34}(F) - L_{36}(S^T) \\ = \gamma_{90} \frac{\partial \ddot{W}}{\partial x} + \gamma_{10} \ddot{\Psi}_x. \end{aligned} \quad (17)$$

$$\begin{aligned} L_{41}(W) - L_{42}(\Psi_x) + L_{43}(\Psi_y) + \gamma_{14} L_{44}(F) - L_{46}(S^T) \\ = \gamma_{90} \beta \frac{\partial \ddot{W}}{\partial y} + \gamma_{10} \ddot{\Psi}_y. \end{aligned} \quad (18)$$

The non-dimensional parameters and nonlinear operator (L) in the equations (15)–(18) are given as follows:

$$\begin{aligned} (x, y, \beta) &= \left(\pi \frac{X}{a}, \pi \frac{Y}{b}, \frac{a}{b} \right), \\ (W, F) &= \left(\frac{\bar{W}}{[D_{11}^* D_{22}^* A_{11}^* A_{22}^*]^{1/4}}, \frac{\bar{F}}{[D_{11}^* D_{22}^*]^{1/2}} \right), \\ (\Psi_x, \Psi_y) &= \frac{a}{\pi} \frac{(\bar{\Psi}_x, \bar{\Psi}_y)}{[D_{11}^* D_{22}^* A_{11}^* A_{22}^*]^{1/4}}, \quad (\gamma_5, \gamma_{14}, \gamma_{24}) \\ &= \left(-\frac{A_{12}^*}{A_{22}^*}, \sqrt{\frac{D_{22}^*}{D_{11}^*}}, \sqrt{\frac{A_{11}^*}{A_{22}^*}} \right), \\ (\gamma_{T1}, \gamma_{T2}) &= \frac{a^2 (A_x^T, A_y^T)}{\pi^2 [D_{11}^* D_{22}^*]^{1/2}}, \\ (\gamma_{T3}, \gamma_{T4}, \gamma_{T6}, \gamma_{T7}) &= \frac{a^2}{\pi^2 h D_{11}^*} \left(D_x^T, D_y^T, \frac{4}{3h^2} F_x^T, \frac{4}{3h^2} F_y^T \right), \\ (M_x, P_x) &= \frac{a^2}{D_{11}^* \pi^2} \frac{1}{[A_{11}^* D_{11}^* A_{22}^* D_{22}^*]^{1/4}} \left(\bar{M}_x, \frac{4}{3h^2} \bar{P}_x \right), \\ (K_1, K_2) &= \frac{a^2}{D_{11}^* \pi^2} (a^2 \bar{K}_1, \bar{K}_2), \\ (k_1, k_2) &= \frac{b^2}{E_0 h^3} (b^2 \bar{K}_1, \bar{K}_2), \quad C_d = \frac{a^3 \bar{C}_d}{\pi^3 D_{11}^*} \sqrt{\frac{E_0}{\rho_0}}, \\ t &= \frac{\pi \bar{t}}{a} \sqrt{\frac{E_0}{\rho_0}}, \quad \gamma_{170} = -\frac{I_1 E_0 a^2}{D_{11}^* \pi^2 \rho_0}, \\ \gamma_{171} &= \frac{4(I_5 I_1 - I_4 I_2) E_0}{3 D_{11}^* h^2 I_1 \rho_0}, \\ (\gamma_{10}, \gamma_{80}, \gamma_{90}) &= (I_{10}, I_8, I_9) \frac{E_0}{\rho_0 D_{11}^*}, \\ (\lambda_x, \lambda_y) &= \frac{(\sigma_x b^2, \sigma_y a^2) h}{4 \pi^2 [D_{11}^* D_{22}^*]^{1/2}}, \\ \lambda_q &= \frac{a^4 Q}{D_{11}^* \pi^4 [A_{11}^* D_{11}^* A_{22}^* D_{22}^*]^{1/4}}, \\ L(\cdot) &= \frac{\partial^2}{\partial X^2} \frac{\partial^2}{\partial Y^2} - 2 \frac{\partial^2}{\partial X \partial Y} \frac{\partial^2}{\partial X \partial Y} + \frac{\partial^2}{\partial Y^2} \frac{\partial^2}{\partial X^2}, \end{aligned} \quad (19)$$

in which the non-dimensional forms of foundation stiffnesses k_1, k_2 are only used in numerical calculations, E_0 and ρ_0 are reference values of matrix Young's modulus and matrix density ρ^m at room temperature, respectively. A_x^T, D_x^T, F_x^T , etc. are defined as follows:

$$\begin{bmatrix} A_x^T & D_x^T & F_x^T \\ A_y^T & D_y^T & F_y^T \end{bmatrix} = - \sum_{k=1}^N \int_{h_{k-1}}^{h_k} (1, Z, Z^3) \begin{bmatrix} A_x \\ A_y \end{bmatrix}_k dZ. \quad (20)$$

In equations (15)–(18), the dimensionless linear operators ($L_{ij}()$) are defined as in Shen [60].

Substitution of dimensionless parameters into equations (14a–b) and (15a–b) yields:

At $x = 0, a$:

$$W = \Psi_y = M_x = P_x = 0, \quad (21a)$$

$$\delta_x = 0, \quad (21b)$$

At $y = 0, b$:

$$W = \Psi_x = M_y = P_y = 0, \quad (21c)$$

$$\delta_y = 0, \quad (21d)$$

where δ_x and δ_y are given as:

$$\begin{aligned} \delta_x = & \frac{1}{4\pi^2\beta^2\gamma_{24}} \int_0^\pi \int_0^\pi \left[\gamma_{24}\beta^2 \frac{\partial^2 F}{\partial y^2} - \gamma_5 \frac{\partial^2 F}{\partial x^2} \right. \\ & + \gamma_{24} \left(\beta\gamma_{223} \frac{\partial \Psi_y}{\partial y} + \gamma_{511} \frac{\partial \Psi_x}{\partial x} \right) \\ & - \gamma_{24} \left(\gamma_{244}\beta^2 \frac{\partial^2 W}{\partial y^2} + \gamma_{611} \frac{\partial^2 W}{\partial x^2} + 2\gamma_{516}\beta \frac{\partial^2 W}{\partial x \partial y} \right) \\ & \left. - \frac{1}{2}\gamma_{24} \left(\frac{\partial W}{\partial x} \right)^2 + (\gamma_{24}^2\gamma_{T1} - \gamma_5\gamma_{T2})\Delta T \right] dx dy, \end{aligned} \quad (22a)$$

$$\begin{aligned} \delta_y = & \frac{1}{4\pi^2\beta^2\gamma_{24}} \int_0^\pi \int_0^\pi \left[\frac{\partial^2 F}{\partial x^2} - \gamma_5\beta^2 \frac{\partial^2 F}{\partial y^2} \right. \\ & + \gamma_{24} \left(\gamma_{220} \frac{\partial \Psi_x}{\partial x} + \gamma_{522}\beta \frac{\partial \Psi_y}{\partial y} \right) \\ & - \gamma_{24} \left(\gamma_{240} \frac{\partial^2 W}{\partial x^2} + \gamma_{622}\beta^2 \frac{\partial^2 W}{\partial y^2} + 2\gamma_{526}\beta \frac{\partial^2 W}{\partial x \partial y} \right) \\ & \left. - \frac{\gamma_{24}\beta^2}{2} \left(\frac{\partial W}{\partial y} \right)^2 + \Delta T(\gamma_{T2} - \gamma_5\gamma_{T1}) \right] dx dy, \end{aligned} \quad (22b)$$

with γ_{ijk} given in Shen [60].

3.2 Solutions for large amplitude vibration

The solutions for equations (15)–(18) consist of an additional and initial displacement terms as a result of the thermal stress. Here, we will only discuss the solution process of the first term. The solutions for the thermal bending can be derived in the same way [61]. The following initial BCs are used in this study:

$$\begin{aligned} \tilde{W}|_{t=0} = \frac{\partial \tilde{W}}{\partial t}|_{t=0} = 0, \quad \tilde{\Psi}_x|_{t=0} = \frac{\partial \tilde{\Psi}_x}{\partial t}|_{t=0} = 0, \\ \tilde{\Psi}_y|_{t=0} = \frac{\partial \tilde{\Psi}_y}{\partial t}|_{t=0} = 0. \end{aligned} \quad (23)$$

Considering $\tau = \varepsilon t$, the equations can be expanded as a function with a small perturbation parameter ε^i (1, 2, 3,...).

$$\begin{aligned} \tilde{W}(x, y, \tau, \varepsilon) &= \varepsilon w_1(x, y, \tau) + \varepsilon^2 w_2(x, y, \tau) \\ &\quad + \varepsilon^3 w_3(x, y, \tau) + \dots \\ \tilde{\Psi}_x(x, y, \tau, \varepsilon) &= \varepsilon \psi_{x1}(x, y, \tau) + \varepsilon^2 \psi_{x2}(x, y, \tau) \\ &\quad + \varepsilon^3 \psi_{x3}(x, y, \tau) + \dots \\ \tilde{\Psi}_y(x, y, \tau, \varepsilon) &= \varepsilon \psi_{y1}(x, y, \tau) + \varepsilon^2 \psi_{y2}(x, y, \tau) \\ &\quad + \varepsilon^3 \psi_{y3}(x, y, \tau) + \dots \\ \tilde{F}(x, y, \tau, \varepsilon) &= f_1(x, y, \tau) + \varepsilon f_2(x, y, \tau) \\ &\quad + \varepsilon^2 f_3(x, y, \tau) + \dots \\ \lambda_q(x, y, \tau, \varepsilon) &= \varepsilon \lambda_1(x, y, \tau) + \varepsilon^2 \lambda_2(x, y, \tau) \\ &\quad + \varepsilon^3 \lambda_3(x, y, \tau) + \dots \end{aligned} \quad (24)$$

Next, an initially deflected hybrid plate is considered and solution of the first-order equation can be assumed to be:

$$w_1(x, y, \tau) = A_{11}^{(1)}(\tau) \sin mx \sin ny, \quad (25)$$

where (m, n) are the half-wave number of vibration mode of plate along the X - and Y -directions, respectively.

Motions equations converted into their perturbation expansions are given from the substitution of solution equation (24) to equations (15)–(18). The perturbation solutions of the motion equations are given below:

$$\begin{aligned} \tilde{W}(x, y, t) &= \varepsilon [A_{11}^{(1)}(t) \sin mx \sin ny] \\ &\quad + \varepsilon^3 [A_{13}^{(3)}(t) \sin mx \sin 3ny \\ &\quad + A_{31}^{(3)}(t) \sin 3mx \sin ny] + O(\varepsilon^4), \end{aligned} \quad (26)$$

$$\begin{aligned} \tilde{\Psi}_x(x, y, t) &= \varepsilon [C_{11}^{(1)}(t) + \ddot{C}_{11}^{(3)}(t)] \cos mx \sin ny \\ &\quad + \varepsilon^2 C_{20}^{(2)}(t) \sin 2mx \\ &\quad + \varepsilon^3 [C_{13}^{(3)}(t) \cos mx \sin 3ny \\ &\quad + C_{31}^{(3)}(t) \cos 3mx \sin ny] + O(\varepsilon^4), \end{aligned} \quad (27)$$

$$\begin{aligned} \tilde{\Psi}_y(x, y, t) &= \varepsilon [D_{11}^{(1)}(t) + \ddot{D}_{11}^{(3)}(t)] \sin mx \cos ny \\ &\quad + \varepsilon^2 D_{02}^{(2)}(t) \sin 2ny \\ &\quad + \varepsilon^3 [D_{13}^{(3)}(t) \sin mx \cos 3ny \\ &\quad + D_{31}^{(3)}(t) \sin 3mx \cos ny] + O(\varepsilon^4), \end{aligned} \quad (28)$$

$$\begin{aligned}
\tilde{F}(x, y, t) = & -B_{00}^{(0)} y^2/2 - b_{00}^{(0)} x^2/2 + \varepsilon[B_{11}^{(1)}(t) \\
& + \ddot{B}_{11}^{(3)}(t)] \cos mx \cos ny \\
& + \varepsilon^2(-B_{00}^{(2)} y^2/2 - b_{00}^{(2)} x^2/2 \\
& + B_{02}^{(2)}(t) \cos 2ny + B_{20}^{(2)}(t) \cos 2mx) \\
& + \varepsilon^3[B_{13}^{(3)}(t) \cos mx \cos 3ny \\
& + B_{31}^{(3)}(t) \cos 3mx \cos ny] + O(\varepsilon^4),
\end{aligned} \quad (29)$$

$$\begin{aligned}
\lambda_q(x, y, t) = & [g_1 A_{11}^{(1)}(t) + g_4 \ddot{A}_{11}^{(1)}(t) \\
& + \varepsilon g_c \dot{A}_{11}^{(1)}(t)] \varepsilon \sin mx \sin ny \\
& + (\varepsilon A_{11}^{(1)}(t))^3 g_3 \sin mx \sin ny + O(\varepsilon^4).
\end{aligned} \quad (30)$$

In equations (26)–(30), τ is replaced back by t and $\varepsilon A_{11}^{(1)}(t)$ is taken as the second perturbation coefficient, which is related to deflection. Here, assuming that $(x, y) = (\pi/2m, \pi/2n)$, $\varepsilon A_{11}^{(1)}(t)$ can be expressed as:

$$\varepsilon A_{11}^{(1)}(t) = \tilde{W}_m - \Theta_1 \tilde{W}_m^3 + \dots \quad (31)$$

Substituting equation (31) into (30) and applying Galerkin procedure yield equation (32), which can be expressed as:

$$\begin{aligned}
g_{40} \frac{d^2(\varepsilon A_{11}^{(1)})}{dt^2} + g_c \frac{d(\varepsilon A_{11}^{(1)})}{dt} + g_{41}(\varepsilon A_{11}^{(1)}) + g_{42}(\varepsilon A_{11}^{(1)})^2 \\
+ g_{43}(\varepsilon A_{11}^{(1)})^3 = \bar{\lambda}_q(t),
\end{aligned} \quad (32)$$

with g_{40} , g_{41} , etc. are given in equations (C.1)–(C.3) of the Appendix C, and

$$\bar{\lambda}_q(t) = \frac{4}{\pi^2} \int_0^\pi \int_0^\pi \lambda_q(x, y, t) \sin mx \sin ny \, dx dy, \quad (33)$$

where $\lambda_q(x, y, t) = \lambda_{q0} F_1(x, y) F_2(t)$. λ_{q0} and $F_1(x, y)$ are the amplitude and distribution function of transvers loading, respectively. $F_2(t)$ is impulsive shapes function, defined in Table 5.

By solving equation (32), the relationship between deflection and time can be obtained to characterize the

forced vibration. It can be easily converted to a free vibration problem by setting the load to zero. Therefore, the solution of the dimensionless nonlinear frequency (ω_{NL}) can be obtained by solving equation (21) with $\bar{\lambda}_q(t) = 0$ can be obtained as follows:

$$\omega_{NL} = \omega_L \left(1 + \frac{9g_{41}g_{43} - 10g_{42}^2}{12g_{41}^2} \frac{\bar{W}_{\max}}{(D_{11}^* D_{22}^* A_{11}^* A_{22}^*)^{1/2}} \right)^{1/2} \quad (34)$$

$$\omega_L = \sqrt{g_{41}/g_{40}}, \quad (35)$$

where ω_L is the dimensionless linear frequency.

3.3 Solutions for forced vibration

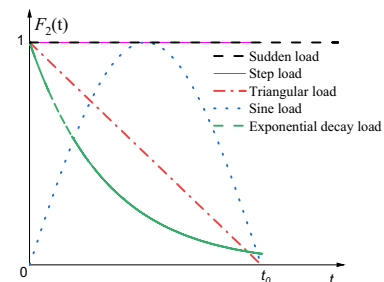
In addition to large amplitude and free vibration analysis, the forced vibration of hybrid laminated plates subjected to dynamic load (see Figure 3) is taken into consideration. The center deflection–time relationship is used to characterize the forced vibration of the plate. Therefore, the second-order ordinary differential equation (see equation 32) with initial value can be obtained using the fourth-order Runge–Kutta method. It is worth noting that the initial deflection for FG- Λ or FG-V will be triggered under the temperature field.

3.4 Solutions for nonlinear bending

In this section, the nonlinear bending response of hybrid laminated plates with NPR and PPR is studied. First, the relationship between the applied pressure and the deflection is determined. For the static analysis, this relationship is independent of the variation in time (t). Therefore, the dynamic load is modified to be static load and $Q(X, Y, t) = q_0$. Based on these assumptions and using a two-step perturbation approach, the solution of motion equations can be obtained as:

Table 5: Impulsive shapes of dynamic loads

Dynamic load	$F_2(t)$
Sudden load	$F_2(t) = 1$
Step load	$F_2(t) = 1, t < t_0$ $F_2(t) = 0, t > t_0$
Triangular load	$F_2(t) = 1 - t/t_0, t < t_0$ $F_2(t) = 0, t > t_0$
Sinusoidal load	$F_2(t) = \sin(\pi t/t_0), t < t_0$ $F_2(t) = 0, t > t_0$
Exponential load	$F_2(t) = e^{-\omega t}$



$$W = \varepsilon A_{11}^{(1)} [\sin mx \sin ny] + (\varepsilon A_{11}^{(1)})^3 [\alpha_{313} \sin mx \sin 3ny + \alpha_{331} \sin 3mx \sin ny] + O(\varepsilon^4), \quad (36)$$

$$\Psi_x = \varepsilon [C_{11}^{(1)} \cos mx \sin ny] + \varepsilon^2 [C_{20}^{(2)} \sin 2mx] + \varepsilon^3 [C_{31}^{(3)} \cos 3mx \sin ny + C_{13}^{(3)} \cos mx \sin 3ny] + O(\varepsilon^4), \quad (37)$$

$$\Psi_y = \varepsilon [D_{11}^{(1)} \sin mx \cos ny] + \varepsilon^2 [D_{02}^{(2)} \sin 2ny] + \varepsilon^3 [D_{13}^{(3)} \sin mx \cos 3ny + D_{31}^{(3)} \sin 3mx \cos ny] + O(\varepsilon^4), \quad (38)$$

$$F = -\left(\frac{B_{00}^{(0)} y^2 + b_{00}^{(0)} x^2}{2}\right) + \varepsilon [B_{11}^{(1)} \sin mx \sin ny] + \varepsilon^2 \left[-\frac{B_{00}^{(2)} y^2 - b_{00}^{(2)} x^2}{2} + B_{20}^{(2)} \cos 2mx + B_{02}^{(2)} \cos 2ny\right] + \varepsilon^3 [B_{31}^{(3)} \sin 3mx \sin ny + B_{13}^{(3)} \sin mx \sin 3ny] + O(\varepsilon^4), \quad (39)$$

and

$$\lambda_q = (\varepsilon A_{11}^{(1)}) \lambda_q^{(1)} + (\varepsilon A_{11}^{(1)})^3 \lambda_q^{(3)} + O(\varepsilon^4). \quad (40)$$

In equations (34)–(37), the second perturbation coefficient $A_{11}^{(1)} \varepsilon$ that relates to the non-dimensional maximum deflection allows the application of a two-step perturbation technology. The load–deflection relationship can be written as:

$$\frac{q_0 a^4}{D_{11}^* h} = A_W^{(1)} \left(\frac{\bar{W}}{h}\right) + A_W^{(3)} \left(\frac{\bar{W}}{h}\right)^3 + \dots \quad (41)$$

It can be noted that $A_W^{(1)}$ and $A_W^{(3)}$ are related to the material properties and are functions of temperature. Further details can be found in Appendix D.

4 Numerical results and discussions

4.1 Validation studies

To verify the proposed model, results of the comparison analysis are reported. The results of four examples are given to validate the present model. Hybrid plates are assumed in the first, second, and fourth examples, whereas FG-CNTRC plates are adopted in the third example.

Example 1. In this example, verification investigations of the free vibration of a simply supported $[\theta^C/90^F]_2$ hybrid plate with $a = 20h$ and $h = 0.5$ mm are presented. Table 6 presents the comparison of the solutions using an analytical model proposed by Fan and Wang [62] and the method presented in this study for a hybrid laminated plate. The two reinforced materials are FRC and CNTRC and the material properties are: (1) for FRC: $E_{11}^F = 233.05$ GPa, $\nu_{12}^F = 0.2$, $E_{22}^F = 23.1$ GPa, $\rho^F = 1,750$ kg/m³, $G_{12}^F = 8.96$ GPa; (2) for CNTRC: $E_{11}^{CN} = 5646.6$ GPa, $\nu_{12}^{CN} = 0.175$, $E_{22}^{CN} = 7080.0$ GPa, $\rho^{CN} = 1,400$ kg/m³, $G_{12}^{CN} = 1944.5$ GPa; for the same matrix: $E^m = 2.5$ GPa, $\rho^m = 1,150$ kg/m³, $\nu^m = 0.34$. The comparison shows that the proposed model has a good agreement with the existing results.

Example 2. This example is given to verify the correctness of the solution for nonlinear vibration of plate. The dimensions of the $(0/90)_{3T}$ plate are: $a = 2b = 20$ mm and $h = 0.6$ mm. Present frequency ratios are compared with those of Pillai and Rao [63] and Lai *et al.* [64] for a plate with $\bar{W}_m/h = 0.5, 1, 1.5, 2$. The determined frequency ratios are then compared with the data in ref. [63,64] and shows an excellent agreement for different deflections (see Figure 4).

Example 3. The predicted dynamic response by the proposed model is compared to the numerical results predicted in detail by Liew *et al.* [65]. The CNTRC plates are set with $a/h = 4$ cm and $b = a$, whereas the material parameters are the same as in Example 1. As shown in Figure 5, the forced vibration curves are compared with the results predicted in ref. [65]. According to the curves plotted in Figure 5, similar trend can be observed between the results.

Example 4. The bending studies of a hybrid plate consisting of a cross-ply $[45^C/-45^F]$ with large deflection are reported by Fan and Wang [66]. A hybrid plate subjected to a uniform and sinusoidal load is considered in the analysis. Constituent materials of the plate are same as in the case of hybrid plates listed in Figure 6. The results of the present dimensionless deflections are compared with those in ref. [66]. As plotted in Figure 6, the proposed results are very close to those presented by Fan and Wang [66].

4.2 Linear vibration analysis

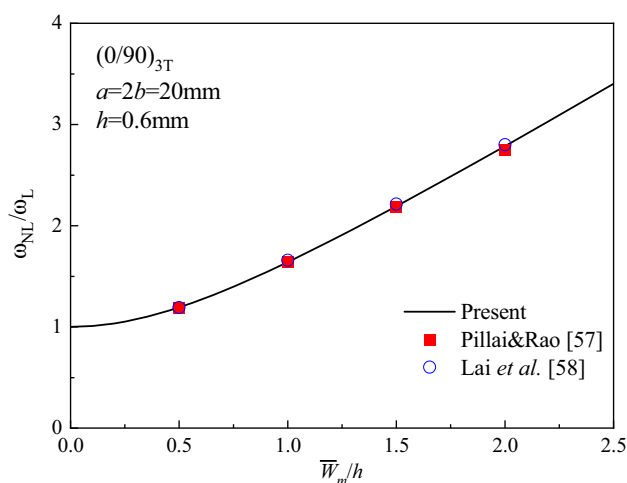
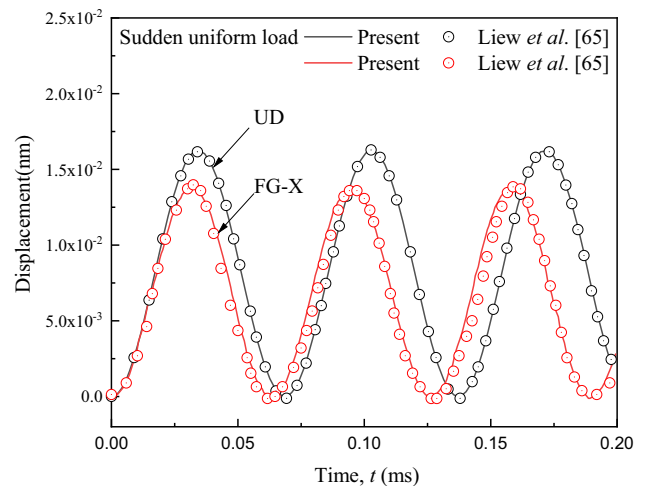
In this subsection, the effects of the change in temperature, CNT distribution pattern, and the foundation

Table 6: Comparison of the fundamental frequencies for $[\theta^C/90^F]_2$ plates

V_{CN}		b/h			
		10	20	50	100
0.12	Fan and Wang [62]	14.8861	16.7109	17.3677	17.4686
	Present	14.6569	16.6273	17.3523	17.4644
0.17	Fan and Wang [62]	16.2484	18.2019	18.8970	19.0034
	Present	16.0858	18.1115	18.8874	19.0072
0.28	Fan and Wang [62]	17.6812	20.2276	21.1827	21.3314
	Present	17.3354	20.0948	21.1646	21.3332

constants (k_1, k_2) on the free vibration of hybrid laminated plates are scrutinized. Unless otherwise specified, the angle-ply $(22^F/(22^C/-22^C)_{3T}/22^F)$ and $(45^F/(45^C/-45^C)_{3T}/45^F)$ hybrid laminated plates are adopted in the following studies.

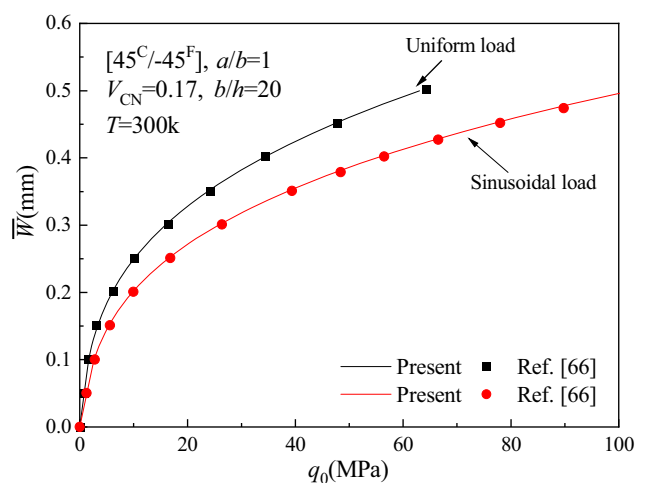
The effect of thermal environments on the first six frequencies $\tilde{\Omega}_{ij}$ ($i, j = 1, 2, 3$) of hybrid laminated plates with five different distribution patterns is investigated in Figure 7(a)–(c). Here, a plate with $(70^F/(70^C/-70^C)_{3T}/70^F)$ is considered for comparison purpose. Among the three angle-ply hybrid plates, the $(45^F/(45^C/-45^C)_{3T}/45^F)$ plates have the maximum first-order frequency for different temperatures. It is observed that increasing the temperature causes decrease in the frequencies for both angle-ply hybrid plates. As a result, the influence of the degradation caused by thermal stress should be taken into consideration in the design and service life of hybrid laminated plates.

**Figure 4:** Comparisons of ω_{NL}/ω_L for angle-ply $(0/90)_{3T}$ laminated plate.**Figure 5:** Comparison of forced vibration curves for UD and FG-X laminated plate.

The values of the stiffnesses in the framework of Pasternak foundation for different distributions of CNT are shown in Figure 7(d) and (e). Two different foundation coefficients (k_1, k_2) are considered, i.e., $(10^2, 10)$, $(10^2, 0)$. It should be noted that structures with $(k_1, k_2) = (0, 0)$ are selected as reference examples and can be found in Figure 7(a). As shown, the natural frequencies of the hybrid laminated plate for higher (k_1, k_2) are greater than the other cases.

4.3 Large amplitude vibration

The nonlinear vibration analysis of hybrid plates is carried out. A non-dimensional frequency ratio (ω_{NL}/ω_L) is

**Figure 6:** Comparison of load–deflection relationships of $[45^C/-45^F]$ plate.

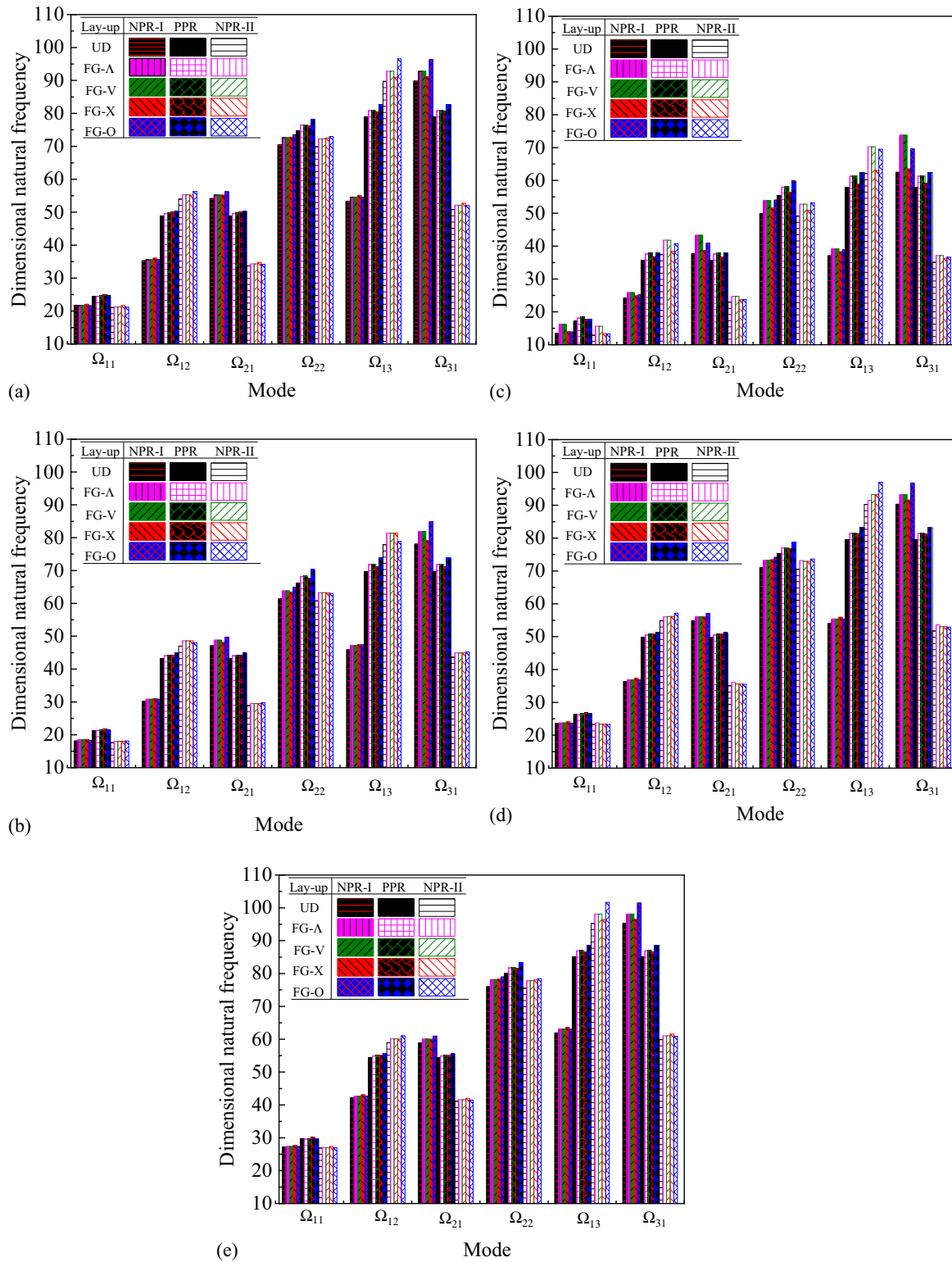


Figure 7: Natural frequencies $\bar{\Omega}_{ij} = \Omega_{ij} b^2 (\rho_0 / E_0)^{0.5} / h$ for different temperatures and foundation stiffness; NPR-I: $(22^F / (22^C / -22^C)_{3T} / -22^F)$, NPR-II: $(70^F / (70^C / -70^C)_{3T} / -70^F)$, PPR: $(45^F / (45^C / -45^C)_{3T} / -45^F)$. (a) $T = 300$ K & $(k_1, k_2) = (0, 0)$; (b) $T = 400$ K & $(k_1, k_2) = (0, 0)$; (c) $T = 500$ K & $(k_1, k_2) = (0, 0)$; (d) $T = 300$ K & $(k_1, k_2) = (100, 0)$; (e) $T = 300$ K & $(k_1, k_2) = (100, 10)$.

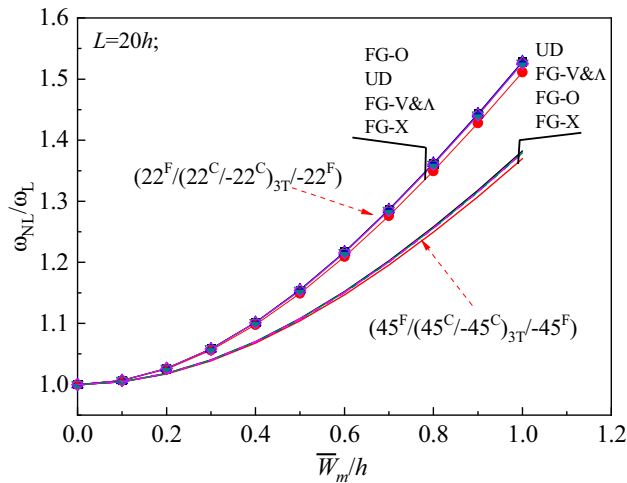


Figure 8: Amplitude curves for hybrid plates with NPR or PPR.

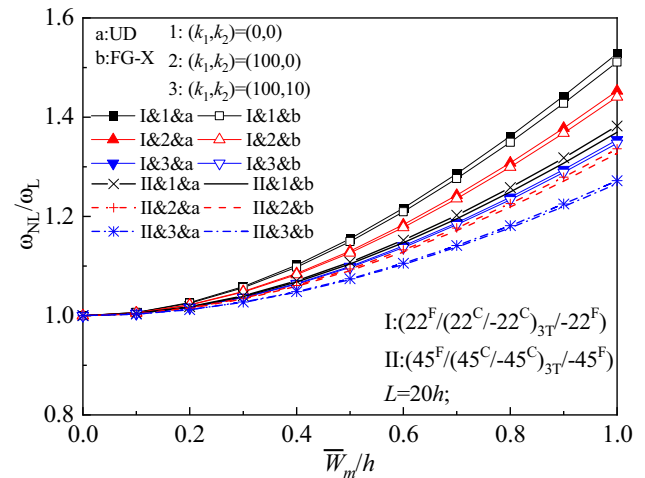


Figure 10: Effect of foundation coefficient on nonlinear vibration for hybrid plates.

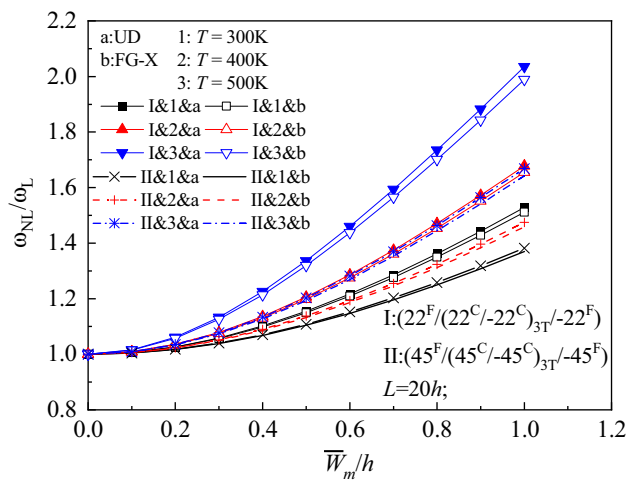
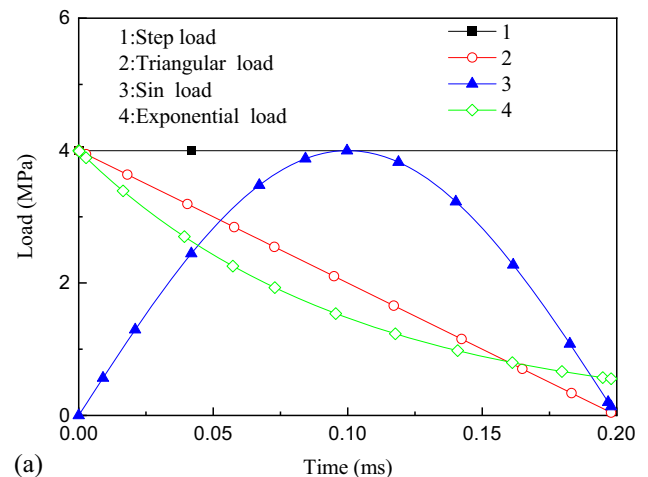


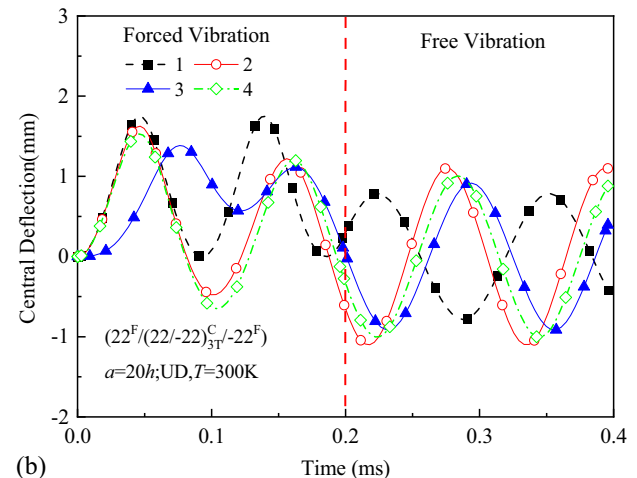
Figure 9: Effect of T on nonlinear vibration for hybrid plates.

considered. The frequency ratio–deflection relationships obtained for hybrid laminated plates composed of CNTRC with different configurations are presented in Figure 8. As expected, FG-X has the lowest frequency ratio, whereas the FG-O has the highest frequency ratio. The frequency ratios for the plate with Λ and V pattern are similar. It shows that the overall stiffness of the plates increases as the CNT volume fraction in the surface layer is increased.

Furthermore, nonlinear frequencies are predicted for UD and FG-X plates subjected to temperatures in the range of 300–500 K. Looking at the curves shown in Figure 9, one can see that an increase in the thermal stress leads to an increase in the frequency ratio. It is found that laminated plates with NPR are more sensitive to temperature changes than plates with PPR.

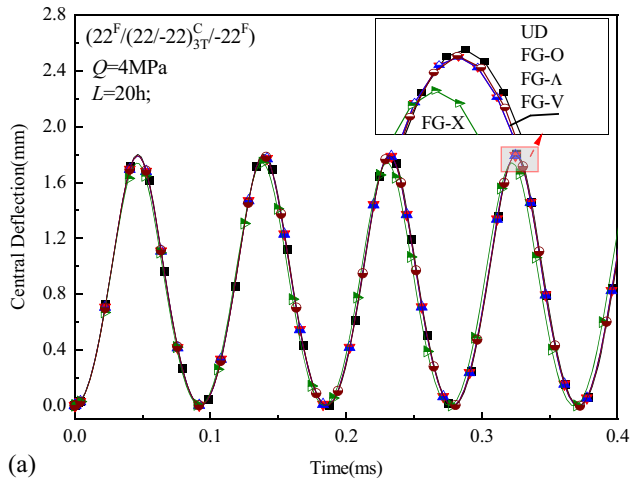


(a)

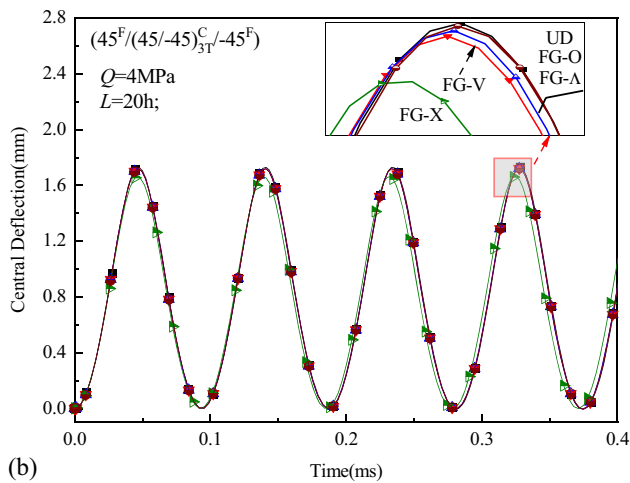


(b)

Figure 11: Effect of dynamic load on forced vibration of hybrid plates. (a) Type of dynamic loads. (b) Vibration curves



(a)



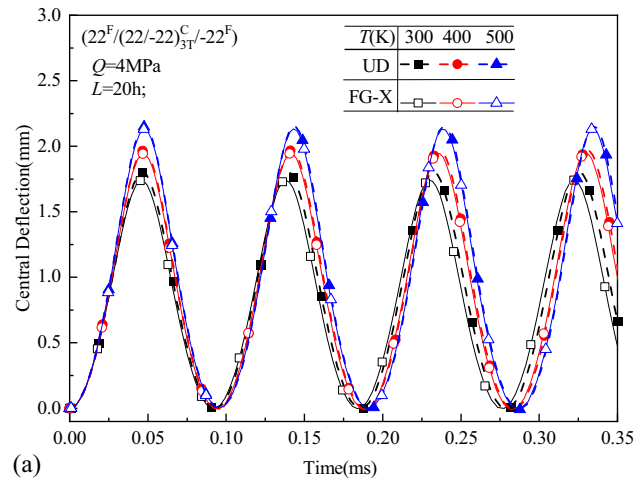
(b)

Figure 12: Forced vibration curves for FG hybrid plates.

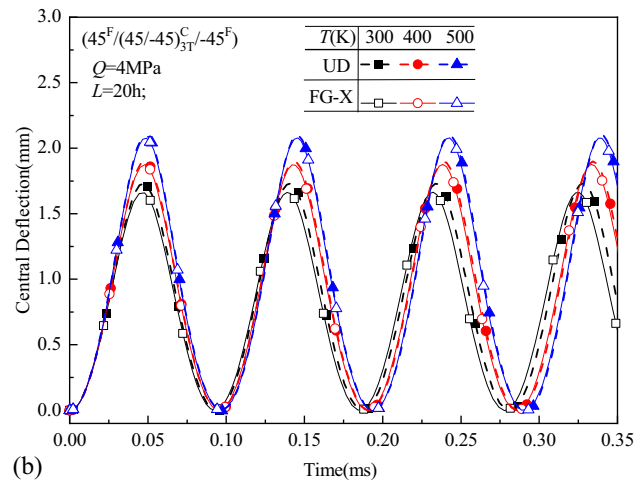
The frequency ratio of UD and FG-X plates with and without considering elastic foundations are obtained as shown in Figure 10. The foundation coefficients are taken as $(k_1, k_2) = (0, 0), (10^3, 0), (10^3, 10)$. From Figure 10, it is concluded that the increase in foundation stiffness makes the plate more rigid when the foundation coefficients of the plate are increased. This also leads to an increase in the frequency ratio of the UD and FG-X. It can also be seen that $(22^F/(22^C/-22^C)_{3T}/-22^F)$ laminated plates are more sensitive to change in foundation stiffnesses than those with $(45^F/(45^C/-45^C)_{3T}/-45^F)$.

4.4 Forced vibration analysis

Hybrid plates with NPR subjected to dynamic load are investigated in this section. Different dynamic loads are adopted to make a comparison and calculate the one corresponding to the maximum deflection of the plate.



(a)



(b)

Figure 13: Effect of T on forced vibration of hybrid laminated plates ($T = 300, 400$, and 500 K).

Except for a sudden load, it is assumed that the duration of the dynamic load is equal to the period of forced vibration. As shown in Figure 11, a comparison of the forced vibration of $(22^F/(22^C/-22^C)_{3T}/-22^F)$ plate with $a = b = 20h$ and $h = 35$ mm subjected to different dynamic loads is proposed. It can be found that the same amplitude does not mean the same deflection of the applied load (Figure 11(b)). The highest deflection is predicted for step load during forced vibration. While analyzing the free vibration of plate, one can find that the highest increment of deflection for the same duration takes place for the triangular load. Unless otherwise specified, a sudden uniform load is considered in the following forced vibration studies.

Five different configurations present above are taken into consideration. The CNT distributions between the central deflection and the time t are analyzed under the reference temperature, and the corresponding curves

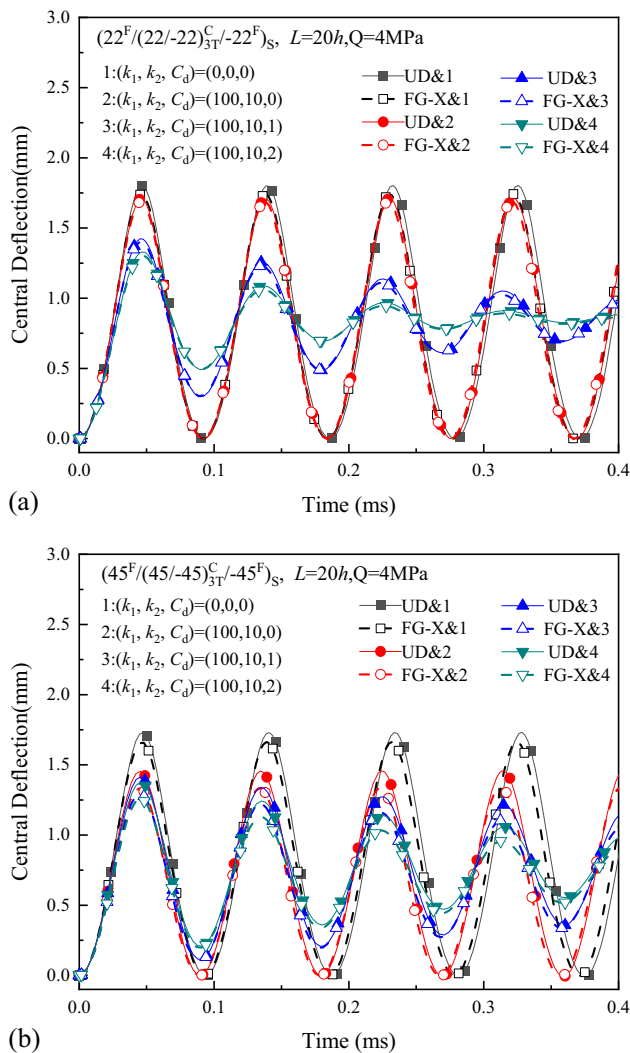


Figure 14: Effect of foundation coefficients on forced vibration of hybrid plates.

are shown in Figure 12(a) and (b). Unless otherwise specified, the amplitude of the load is fixed at 4 MPa. As expected, the type of FG configurations has a considerable effect on the forced vibration. Furthermore, FG-X exhibits great stiffness, which can be attributed to the increased V_{CN} near the top and bottom layers. Thus, for the next parametric analysis, the studying examples are taken as UD and FG-X.

In Figure 13(a) and (b), the influence because of variation in thermal stress is considered in the forced vibration of the UD and FG-X plates. The applied uniform load is adopted as 4 MPa for $(22^F/(22^C/-22^C)_{3T}/-22^F)$ and $(45^F/(45^C/-45^C)_{3T}/-45^F)$ with $L = 20h$. It is found that the deflection and period of plate increase with increase in thermal stress. In fact, this phenomenon may be attributed to

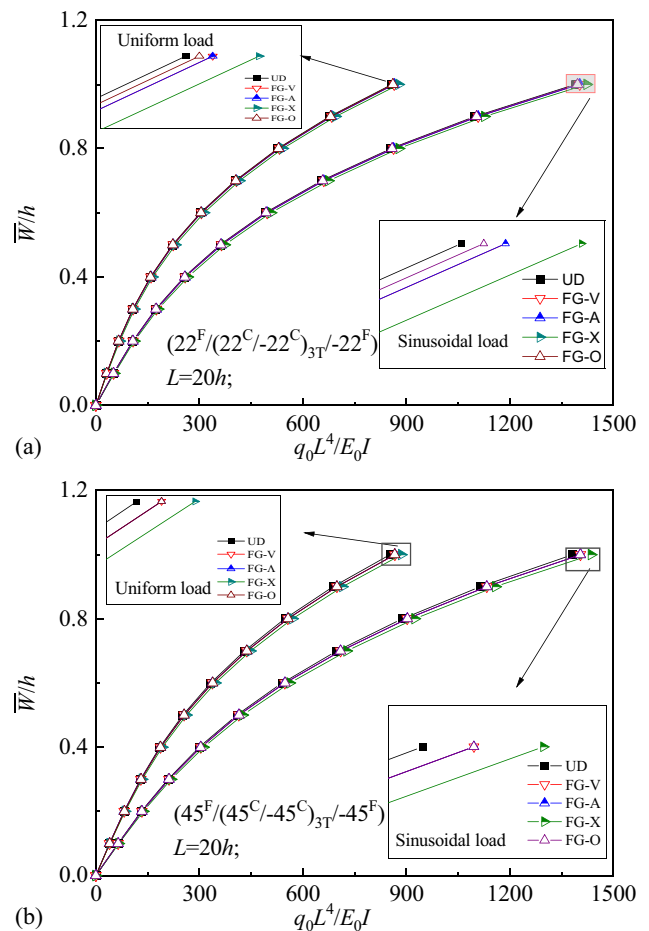


Figure 15: Load versus deflection of hybrid laminated plate composed of different CNT distribution patterns.

reduction in the overall stiffness of the plates under thermal environment.

Figure 14(a) and (b) show the variation in maximum deflections with time for hybrid plates $(22^F/(22^C/-22^C)_{3T}/-22^F)$ and $(45^F/(45^C/-45^C)_{3T}/-45^F)$ for different foundation stiffnesses, but for the same temperature. To evaluate the influence of Pasternak and viscoelastic foundation, the plates with $k_1 = k_2 = C_d = 0$ are adopted for comparative analysis. It appears that the dynamic behavior of the plates depends significantly on the values of the foundation coefficients. For example, the value of central deflections decreases with an increase in the foundation coefficient. The reinforcement effect of viscoelastic foundation is more obvious as compared to elastic foundation. It means that the forced vibration of the hybrid laminated plates is significantly influenced by the viscoelastic parameter. Furthermore, the peak value of the central deflection decreases with increase in time.

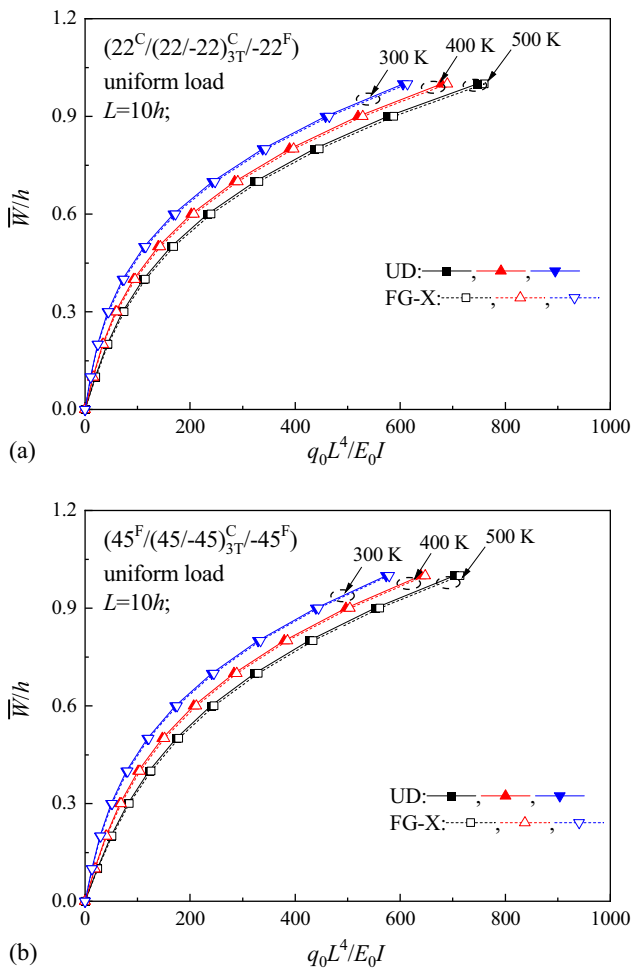


Figure 16: Effect of thermal field on bending behavior of hybrid laminated plates.

4.5 Nonlinear bending analysis

Figure 15(a) and (b) illustrate the nonlinear bending curves for UD and FG-plates subjected to different loading scenarios. Under uniform and sinusoidal distribution load, it is found that the deflection of FG-O plate is largest, followed by UD. In addition, FG-X plates exhibit the largest bearing capacity. This is because CNTs are distributed away from the interlayer to improve the bending stiffness of the plate. Therefore, in the following, exhaustive studies will be carried out to evaluate the bending performance of FG-X and UD subjected to UD load, and different environmental conditions.

To evaluate the influence of thermal environment on the bending characteristics of FRC/CNTRC hybrid plate, Figure 16(a) and (b) show the variations in the central

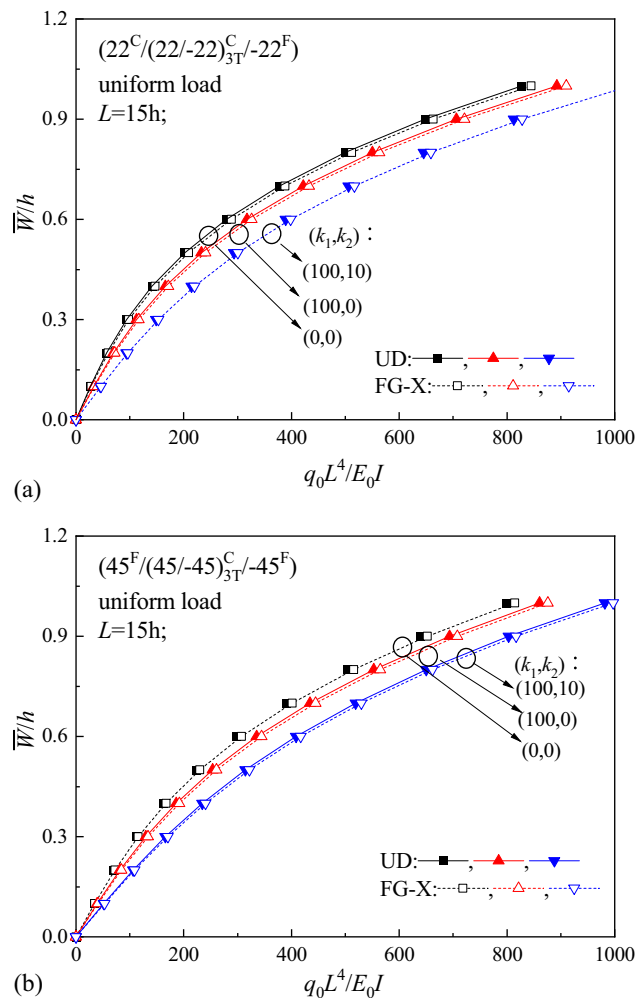


Figure 17: Effect of foundation coefficient on bending behavior of hybrid laminated plates.

deflection of UD and FG-X plates with $L = 10h$ versus load for various temperature fields. It is easy to observe that the deflection of the hybrid laminated plates increases with increment of temperature. As a result, the effect of the degradation caused by temperature field should be considered in the design of bearing capacity of plates.

Figure 17(a) and (b) show the influence of the foundation coefficients on the bending behavior of UD and FG-X with room temperature and $L = 20h$. Three sets of values are selected for the stiffnesses of the elastic foundation $((k_1, k_2) = (0, 0), (10^2, 0), (10^2, 10))$. As expected, the central deflection decreases when the foundation stiffness is increased.

5 Closing remarks

In this study, static and dynamic characteristics of hybrid plates fabricated from FRC layer and FG-CNTRC core resting on elastic foundation are studied. According to the arrangement of CNT, four FG distributions (Λ , V, X, O) and UD are taken into consideration. For the configurations of $(22^F/(22^C/-22^C)_{3T}/-22^F)$ and $(45^F/(45^C/-45^C)_{3T}/-45^F)$, the out-of-plane Poisson's ratios exhibit NPR and PPR, respectively. A two-step perturbation technology is adopted to solve the bending and vibration problem of the above plates. Geometric nonlinear analysis is performed by investigating large amplitude vibration, forced vibration, and bending situations. The influence of the variation in the thermal stress and the foundation stiffness on the static and dynamic characteristics of FRC/CNTRC laminated plates are also studied.

The following observations are summarized from the present study:

- The configuration of CNTs has significant effect on the mechanical response of hybrid plate. The results show that FG-X arrangement exhibits minimum central deflection or nonlinear vibration frequency under the reference temperature. Moreover, FG-X configuration still shows excellent performance in thermal environment and foundation conditions.
- It is observed that environmental conditions have a considerable effect on the frequency of plates. Increasing the foundation coefficients (k_1 , k_2) increases the frequencies of hybrid plates, whereas the elevated temperature effect plays an opposite role on the vibration behavior of these members.
- In the case of nonlinear bending, vibration, and forced vibration behavior, increasing thermal stresses will increase the central deflection and nonlinear vibration frequency, whereas increasing the value of (k_1 , k_2) will lead to an opposite effect.
- The most dangerous function shape loading is the step load. It gives the highest deflection for all the analyzed cases. For viscoelastic foundation, a larger difference in the middle deflection is visible for the duration greater than 0.5 ms.
- The results of the parametric analysis reveal that the large amplitude vibration of $(22^F/(22^C/-22^C)_{3T}/-22^F)$ laminated plates is more sensitive to variation in the temperature and foundation stiffness as compared to those with $(45^F/(45^C/-45^C)_{3T}/-45^F)$.

Acknowledgments: The authors are grateful for the support from the Science Research Plan of Shanghai Municipal

Science and Technology Committee under Grant 18DZ1205603, National Natural Science Foundation of China [Grant No. 52078293, 51908352, 51978330, 51808286], and Natural Science Foundation of Jiangsu Province [Grant No. BK20180710].

Conflicts of interest: The authors declare no conflict of interest regarding the publication of this paper.

References

- [1] Grima JN, Gatt R, Ellul B, Chetcuti E. Auxetic behaviour in non-crystalline materials having star or triangular shaped perforations. *J Non-Cryst Solids*. 2010;356(37–40):1980–7.
- [2] Ren X, Shen J, Ghaedizadeh A, Tian H, Min Xie Y. Experiments and parametric studies on 3D metallic auxetic metamaterials with tuneable mechanical properties. *Smart Mater Struct*. 2015;24(9):95016.
- [3] Ren X, Shen J, Ghaedizadeh A, Tian H, Xie YM. A simple auxetic tubular structure with tuneable mechanical properties. *Smart Mater Struct*. 2016;25(6):65012.
- [4] Ren X, Das R, Tran P, Ngo TD, Xie YM. Auxetic metamaterials and structures: a review. *Smart Mater Struct*. 2018;27(2):23001.
- [5] Alderson KL, Coenen VL. The low velocity impact response of auxetic carbon fibre laminates. *Phys Status Solidi B*. 2008;245(3):489–96.
- [6] Zhou L, Zeng J, Jiang L, Hu H. Low-velocity impact properties of 3D auxetic textile composite. *J Mater Sci*. 2018;53(5):3899–914.
- [7] Madke RR, Chowdhury R. Anti-impact behavior of auxetic sandwich structure with braided face sheets and 3D re-entrant cores. *Compos Struct*. 2020;236:111838.
- [8] Chang Y, Ma P, Jiang G. Energy absorption property of warp-knitted spacer fabrics with negative Poisson's ratio under low velocity impact. *Compos Struct*. 2017;182:471–7.
- [9] Li D, Yin J, Dong L, Lakes RS. Numerical analysis on mechanical behaviors of hierarchical cellular structures with negative Poisson's ratio. *Smart Mater Struct*. 2017;26(2):25014.
- [10] Lim TC. Shear deformation in rectangular auxetic plates. *J Eng Mater Technol*. 2014;136(3):1–6.
- [11] Behravan Rad A. Static analysis of non-uniform 2D functionally graded auxetic-porous circular plates interacting with the gradient elastic foundations involving friction force. *Aerosp Sci Technol*. 2018;76:315–39.
- [12] Chen X, Feng ZH. Dynamic behaviour of a thin laminated plate embedded with auxetic layers subject to in-plane excitation. *Mech Res Commun*. 2017;85:45–52.
- [13] Asemi K, Shariyat M. Three-dimensional biaxial post-buckling analysis of heterogeneous auxetic rectangular plates on elastic foundations by new criteria. *Comput Method Appl M*. 2016;302:1–26.
- [14] Mansouri MH, Shariyat M. Differential quadrature thermal buckling analysis of general quadrilateral orthotropic auxetic FGM plates on elastic foundations. *Thin Wall Struct*. 2017;112:194–207.

- [15] Mansouri MH, Shariyat M. Biaxial thermo-mechanical buckling of orthotropic auxetic FGM plates with temperature and moisture dependent material properties on elastic foundations. *Compos Part B Eng.* 2015;83:88–104.
- [16] Evans KE, Donoghue JP, Alderson KL. The design, matching and manufacture of auxetic carbon fibre laminates. *J Compos Mater.* 2004;38(2):95–106.
- [17] Zhang RG, Yeh HL, Yeh HY. A preliminary study of negative Poisson's ratio of laminated fiber reinforced composites. *J Reinf Plast Comp.* 1998;17(18):1651–64.
- [18] Herakovitch CT. Composite laminates with negative through-the-thickness. *J Compos Mater.* 1984;18(5):447–55.
- [19] Hine PJ, Duckett RA, Ward IM. Negative Poisson's ratios in angle-ply laminates. *J Mater Sci Lett.* 1997;16(7):541–4.
- [20] Matsuda T, Goto K, Kubota N, Ohno N. Negative through-the-thickness Poisson's ratio of elasti-viscoplastic angle-ply carbon fiber-reinforced plastic laminates: homogenization analysis. *Int J Plast.* 2014;63:152–69.
- [21] Hadi Harkati EL, Bezazi A, Scarpa F, Alderson K, Alderson A. Modelling the influence of the orientation and fibre reinforcement on the negative Poisson's ratio in composite laminates. *Phys Status Solidi B.* 2007;244(3):883–92.
- [22] Hadi Harkati E, Bezazi A, Boukharouba W, Scarpa F. Influence of carbon fibre on the through-the-thickness NPR behaviour of composite laminates. *Phys Status Solidi B.* 2009;246(9):2111–7.
- [23] Sun CT, Li SJ. Three-dimensional effective elastic constants for thick laminates. *J Compos Mater.* 1988;22(7):629–39.
- [24] Shen HS. Nonlinear bending of functionally graded carbon nanotube-reinforced composite plates in thermal environments. *Compos Struct.* 2009;91(1):9–19.
- [25] Shen HS, Huang XH, Yang J. Nonlinear bending of temperature-dependent FG- CNTRC laminated plates with negative Poisson's ratio. *Mech Adv Mater Struc.* 2020;27(13):1–13.
- [26] Shen HS, Li C, Reddy JN. Large amplitude vibration of FG- CNTRC laminated cylindrical shells with negative Poisson's ratio. *Comput Method Appl M.* 2019;360:112727.
- [27] Fan Y, Wang Y. The effect of negative Poisson's ratio on the low-velocity impact response of an auxetic nanocomposite laminate beam. *Int J Mech Mater Des.* 2020. doi: 10.1007/s10999-020-09521-x.
- [28] Yang J, Huang XH, Shen HS. Nonlinear vibration of temperature-dependent FG-CNTRC laminated beams with negative Poisson's ratio. *Int J Struct Stab Dy.* 2020;20(4):2050043.
- [29] Chen H, Song H, Li Y, Safarpour M. Hygro-thermal buckling analysis of polymer-CNT-fiber-laminated nanocomposite disk under uniform lateral pressure with the aid of GDQM. *Eng Comput.* 2020. doi: 10.1007/s00366-020-01102-y.
- [30] Fu T, Wu X, Xiao Z, Chen Z. Dynamic instability analysis of porous FGM conical shells subjected to parametric excitation in thermal environment within FSDT. *Thin Wall Struct.* 2021;158:107202.
- [31] Fu T, Wu X, Xiao Z, Chen Z. Dynamic instability analysis of FG-CNTRC laminated conical shells surrounded by elastic foundations within FSDT. *Eur J Mech A Solid.* 2021;85:104139.
- [32] Yang J, Huang XH, Shen HS. Nonlinear flexural behavior of temperature-dependent FG-CNTRC laminated beams with negative Poisson's ratio resting on the Pasternak foundation. *Eng Struct.* 2020;207:110250.
- [33] Huang XH, Yang J, Bai L, Wang X, Ren X. Theoretical solutions for auxetic laminated beam subjected to a sudden load. *Structures.* 2020;28:57–68.
- [34] Yu Y, Shen HS. A comparison of nonlinear vibration and bending of hybrid CNTRC/metal laminated plates with positive and negative Poisson's ratios. *Int J Mech Sci.* 2020;183:105790.
- [35] Fan Y, Wang H. Nonlinear vibration of matrix cracked laminated beams containing carbon nanotube reinforced composite layers in thermal environments. *Compos Struct.* 2015;124:35–43.
- [36] Fan Y, Wang H. Nonlinear low-velocity impact on damped and matrix-cracked hybrid laminated beams containing carbon nanotube reinforced composite layers. *Nonlinear Dyn.* 2017;89(3):1863–76.
- [37] Lei ZX, Yin BB, Liew KM. Bending and vibration behaviors of matrix cracked hybrid laminated plates containing CNTR-FG layers and FRC layers. *Compos Struct.* 2018;184:314–26.
- [38] Lei ZX, Zhang LW, Liew KM. Modeling large amplitude vibration of matrix cracked hybrid laminated plates containing CNTR-FG layers. *Appl Math Model.* 2018;55:33–48.
- [39] Lei ZX, Yang Z. Characterizing buckling behavior of matrix-cracked hybrid plates containing CNTR-FG layers. *Steel Compos Struct.* 2018;28(4):495–508.
- [40] Kamarian S, Shakeri M, Yas MH. Natural frequency analysis and optimal design of CNT/fiber/polymer hybrid composites plates using mori-tanaka approach, GDQ technique, and firefly algorithm. *Polym Compos.* 2018;39(5):1433–46.
- [41] Pan ZZ, Chen XH, Zhang LW. Modeling large amplitude vibration of pretwisted hybrid composite blades containing CNTRC layers and matrix cracked FRC layers. *Appl Math Model.* 2020;83:640–59.
- [42] Zhang LW, Pan ZZ, Chen XH. Vibration characteristics of matrix cracked pretwisted hybrid composite blades containing CNTRC layers. *J Sound Vib.* 2020;473:115–35.
- [43] Kuo S. Vibration of thermally post-buckled hybrid laminates with two non-uniformly distributed fibers. *Thin Wall Struct.* 2017;114:70–9.
- [44] Papa I, Boccarusso L, Langella A, Lopresto V. Carbon/glass hybrid composite laminates in vinylester resin: bending and low velocity impact tests. *Compos Struct.* 2020;232:111571.
- [45] Lee S, Hwang J. Finite element nonlinear transient modelling of carbon nanotubes reinforced fiber/polymer composite spherical shells with a cutout. *Nanotechnol Rev.* 2019;8(1):444–51.
- [46] Behdinan K, Moradi-Dastjerdi R, Safaei B, Qin Z, Chu F, Hui D. Graphene and CNT impact on heat transfer response of nanocomposite cylinders. *Nanotechnol Rev.* 2020;9(1):41–52.
- [47] Hui Y, Giunta G, Belouettar S, Huang Q, Hu H, Carrera E. A free vibration analysis of three-dimensional sandwich beams using hierarchical one-dimensional finite elements. *Compos Part B Eng.* 2017;110:7–19.
- [48] Wang X, Yang J, Liu Q, Zhang Y, Zhao C. A comparative study of numerical modelling techniques for the fracture of brittle materials with specific reference to glass. *Eng Struct.* 2017;152:493–505.
- [49] Wu Y, Liu Q, Fu J, Li Q, Hui D. Dynamic crash responses of bio-inspired aluminum honeycomb sandwich structures with CFRP panels. *Compos Part B Eng.* 2017;121:122–33.
- [50] Hung P, Lau K, Cheng L, Leng J, Hui D. Impact response of hybrid carbon/glass fibre reinforced polymer composites

- designed for engineering applications. *Compos Part B Eng.* 2018;133:86–90.
- [51] Wang X, Yang J, Liu Q, Zhao C. Experimental investigations into SGP laminated glass under low velocity impact. *Int J Impact Eng.* 2018;122:91–108.
- [52] Zhang LW, Memar Ardestani M, Liew KM. Isogeometric approach for buckling analysis of CNT-reinforced composite skew plates under optimal CNT-orientation. *Compos Struct.* 2017;163:365–84.
- [53] Jam JE, Maghamikia S. Elastic buckling of composite plate reinforced with carbon nanotubes. *J Eng Sci Technol.* 2011;3(1):4090–101.
- [54] Reddy JN. *Mechanics of laminated composite plates: theory and analysis.* Boca Raton, FL: CRC Press; 1997.
- [55] Huang XH, Yang J, Wang X, Azim I. Combined analytical and numerical approach for auxetic FG-CNTRC plate subjected to a sudden load. *Eng Comput.* 2020. doi: 10.1007/s00366-020-01106-8.
- [56] Nettles AT. *Basic mechanics of laminated composite plates.* United States: NASA; 1994.
- [57] Shen HS. Hygrothermal effects on the postbuckling of shear deformable laminated plates. *Int J Mech Sci.* 2001;43(5):1259–81.
- [58] Yeh HL, Yeh HY. Transverse moduli effect on dilatation and through-thickness Poisson's ratio of composite laminates. *J Reinf Plast Comp.* 2001;20(12):1066–85.
- [59] Reddy JN. A simple higher-order theory for laminated composite plates. *J Appl Mech.* 1984;51(4):745–52.
- [60] Shen HS. *A two-step perturbation method in nonlinear analysis of beams, plates and shells.* Singapore: John Wiley & Sons Inc; 2013.
- [61] Yang J, Huang XH, Shen HS. Nonlinear vibration of temperature-dependent FG-CNTRC laminated plates with negative Poisson's ratio. *Thin Wall Struct.* 2020;148:106514.
- [62] Fan Y, Wang H. Nonlinear dynamics of matrix-cracked hybrid laminated plates containing carbon nanotube-reinforced composite layers resting on elastic foundations. *Nonlinear Dyn.* 2016;84(3):1181–99.
- [63] Pillai SRR, Rao NB. Reinvestigation of non-linear vibration of simply supported rectangular cross-ply plates. *J Sound Vib.* 1993;160:1–6.
- [64] Lai SK, Lim CW, Xiang Y, Zhang W. On asymptotic analysis for large amplitude nonlinear free vibration of simply supported laminated plates. *J Vib Acoust.* 2009;131:51010.
- [65] Lei ZX, Zhang LW, Liew KM. Elastodynamic analysis of carbon nanotube-reinforced functionally graded plates. *Int J Mech Sci.* 2015;99:208–17.
- [66] Fan Y, Wang H. Nonlinear bending and postbuckling analysis of matrix cracked hybrid laminated plates containing carbon nanotube reinforced composite layers in thermal environments. *Compos Part B Eng.* 2016;86:1–16.
- [67] Shen H. Kármán-type equations for a higher-order shear deformation plate theory and its use in the thermal postbuckling analysis. *Appl Math Mech.* 1997;18(12):1137–52.